# ASSESSMENT OF AEROMECHANICS AND ACOUSTICS METHODS FOR BVI PREDICTION USING CFD

R. Boisard, M. Costes, G. Reboul, F. Richez, B. Rodriguez
ONERA - The French Aerospace Lab
F-92190 Chatillon, France

**From 2006 to 2012, the French SHANEL project (Simulation of Helicopter Aerodynamics, Noise and ELasticity) considered BVI (Blade Vortex Interaction) noise predictions using advanced CFD methods. Within this six years project, particular were put both into accurate blade deformation prediction and rotor blade tip vortex capturing and conservation in order to improve BVI noise prediction. While blade tip vortex conservation can be highly improved by reducing the mesh cell size, the main drawback is an important increase of the number of mesh points and therefore in computational time. In this study the alternative vorticity confinement method is studied. The use of the vorticity confinement method in the CFD solver avoids blade tip vortex dissipation and keeps strong blade vortex interactions even on a less refined mesh. This method was applied on different HARTII test cases and on the more advanced geometry rotor: ERATO. For all rotors and flight conditions studied, it shows its ability to produce good aerodynamic and noise predictions while keeping the computational cost to an acceptable level.**

## 1. INTRODUCTION

The numerical simulation of rotorcraft aerodynamics, dynamics and acoustics still remains challenging, requiring the use of advanced numerical techniques. The flowfield around helicopters is characterized by large regions of vortical flow that lead to multiple interactions between the airframe components and the rotor itself. Wake and vortices behind each rotor blade are particularly important since they directly interact with the other blades producing the so called BVI (Blade Vortex Interaction) noise which restrains the use of helicopters in urban environment. BVI is relatively difficult to predict since it requires an accurate capture and conservation of the blade tip vortex during several revolutions, coupled to an accurate blade deformation prediction. This challenge was particularly addressed in the French SHANEL project from 2006 to 2012 [1].

The present study will focus on capturing by CFD the aerodynamics of blade vortex interactions and its acoustic radiation using a loosely coupled trim and blade deformation from a dynamic comprehensive code for a rotor in descent flight conditions. Usually, CFD approaches require a very fine mesh in order to accurately capture the rotor wake geometry. However fine meshes always involve large computation time that may not be acceptable within a design process. In a first step, a reference computation will be performed on such a refined mesh for the BO105 rotor in descent flight condition which features strong BVI interactions. Then, an alternative method will be investigated in order to reduce the computational cost while keeping the aerodynamic and acoustic prediction to an acceptable level. The mesh cell size is increased in combination of the use of the vorticity confinement method in the CFD solver to avoid blade tip vortex dissipation. Both computations are performed on the well known HARTII baseline case. This enables assessing the accuracy of vorticity confinement method, not only by comparing the results to the refined mesh computation but also to the experimental database. The robustness and accuracy of this approach is also assessed by further experimental comparisons. Two other comparisons are then performed on the minimum noise and minimum vibration cases from HARTII test campaign, which feature 3/rev higher harmonic blade root pitch control (HHC). An additional computation is done for an advanced rotor geometry (ERATO rotor, which features a doubly swept planform) and compared to experimental results.

## 2. NUMERICAL METHODS

All the computations performed in this work are based on a computational fluid dynamics solver coupled with a comprehensive helicopter dynamics code in order to provide aeroelastic simulations.

## 2.1. Aerodynamic Methods

All the unsteady computations from this study were performed with ONERA's elsA CFD solver [2]. This multi- application CFD software solves the Reynolds averaged Navier-Stokes equations relying on a cell-centred finite volume formulation for structured meshes, including overset and patched grid capabilities.

In the present work, the spatial discretization of the equations is achieved thanks to the second order centered Jameson's scheme with scalar artificial viscosity and Martinelli's correction. The time scheme used is a backward Euler scheme with LU-relax decomposition for inverting the implicit part of the time discretization. To capture high frequencies due to BVI, the constant time step used correspond to a variation of 0.3° of azimuth per time step combined to 15 Newton sub-iterations of the Gear equation. The turbulence model used is K-w Wilcox with Zheng limiter and SST correction.

### 2.1.1. Vorticity Confinement

Vorticity Confinement has been introduced by Steinhoff et al for wake conservation in an Eulerian resolution of the fluid-dynamics equations. It consists in adding a source term into the momentum equation, in order to counteract the spurious dissipation of vorticity by numerical discretization. Two VC schemes have been proposed by Steinhoff, called VC1 [3] and VC2 [4]. Both have also been investigated at ONERA, and in this work the VC2 scheme is selected for its better numerical properties, namely its conservativity and its regularity at vortex centres [5]. Considering the momentum equation with VC:

$$\frac{d\vec{U}}{dt} + \frac{1}{\rho}\vec{\nabla}p - \frac{1}{\rho}\vec{\nabla}\cdot\bar{\bar{\tau}} = \vec{f}$$

the VC2 term is given by:

$$\vec{f} = -\vec{\nabla}\times\left(\mu\vec{\omega} - \varepsilon\vec{w}\right)$$

VC2 is thus the curl of the sum of two vectors: the first one is the vorticity vector and the resulting source term is dissipative, while the second one is aligned with vorticity, of magnitude equal to the harmonic mean of the vorticity modulus of the surrounding grid points, and it introduces negative dissipation in the discretization:

$$\vec{w} = \frac{\vec{\omega}}{\omega}\left[\frac{\sum_{l=1}^{N}(\omega_l)^{-1}}{N}\right]^{-1} = h(\omega_1 ... \omega_N)\frac{\vec{\omega}}{\omega}$$

The dissipative and negative dissipation properties of these two contributions can be easily derived from the vorticity transport equation, obtained by taking the curl of the momentum equation (see [6] for details). Both terms depend on empirical parameters μ and ε, which are user-defined. For consistency, both coefficients are also prescribed to be proportional to the mesh size, in conformity with a 1D analysis of VC2. Neglecting the numerical dissipation of the numerical discretization without confinement, the profile of the computed vortices then depends on the ratio ε/μ. Finally, the use of confinement requires a selection of the areas of the flow-field where VC2 is applied. This is done by using the Q criteria, in order to avoid the application of confinement inside boundary layers. Practically, a threshold value on the Q criteria is defined, and all areas of the flow-field above this threshold value are confined by the VC2 scheme.

## 2.2. Blade Dynamics

Throughout this paper, the blade dynamics is provided by the HOST code (Helicopter Overall Simulation Tool) [7]. This comprehensive code was developed by Eurocopter France in order to simulate and analyse the behaviour of an isolated rotor or a complete helicopter. The blade dynamics is described by beam theory with modal decomposition in order to reduce the number of unknowns. For the blade aerodynamics, it uses a simplified model based on blade element theory with 2D airfoil tables. Several wake models based on a Lagrangian approach are available in HOST, ranging from a simple prescribed wake to an unsteady free wake model without any periodic assumption.

For computing the rotor, two different methodologies can be used in HOST. The trim solution, valid for steady flight conditions, makes the assumption that the flow is periodic in time, so that all rotor parameters can be decomposed into Fourier series in order to reduce the number of unknowns. The rotor solution is then obtained for user-prescribed trim conditions. This is the approach used in loose coupling computations. The other approach works in the time domain. Starting from a trimmed solution, the fluid – structure problem is solved in a time-marching

approach. It is typically what is used in strong coupling computations.

In this study, elsA and HOST are coupled using the loose coupling approach [8]. The CFD loads from elsA and blade kinematics from HOST are exchanged at each rotor revolution. At each iteration, aerodynamic forces from HOST simplified model are corrected by the forces from the CFD computation. From these aerodynamic loads, HOST computes the generalized coordinates of the structure and then by combination of the corresponding modal shapes, provides the dynamic response and deformations of the blade in flap, lag and torsion to the deformation module of the CFD solver. At convergence of the loose coupling, the CFD loads replace totally the comprehensive code aerodynamic loads.

## 2.3. Acoustic Methods

The acoustic predictions methodology consists in a direct post-processing of CFD fields computed by elsA using the code KIM [9][10] based on integral methods. The Ffowcs-Williams and Hawkings (FW-H) [11] formulation is used by considering the blade surfaces as integration surfaces. By doing so, we consider that the noise radiation is composed of the thickness noise due to the blade displacement in the air and of the loading noise due to pressure fluctuations on the blades surfaces. Quadrupolar noise sources possibly present in the volume surrounding the blades are neglected. This is justified by the fact that we are focusing on the Blade Vortex Interaction (BVI) occurring during low speed descent flight. This phenomenon is responsible of intense and impulsive pressure fluctuations on the blades and no quadrupolar sources are expected in the fluid around the blades because of the low Mach number. On the contrary, the quadrupolar noise becomes dominant in high speed cases [12] with transonic tip speed.

# 3. EFFECTS OF MODELLING ON BVI

The validation of vorticity confinement method for cheaper, nonetheless accurate, BVI noise predictions was performed using the HARTII baseline descent flight case. Aerodynamic and acoustic predictions obtained with VC2 are compared to both experimental data and a reference computation.

## 3.1. HARTII Test Case

The second Higher Harmonic Control Acoustic Rotor Test (HART II, [13]) took place in 2001 in the 8m x 6m open jet LLF facility of the German Dutch wind tunnel (DNW) as a cooperative American, French, German, Dutch effort (Figure 1). The experiment involved a Mach scaled BO105 rotor blade. The BO105 rotor is a four rectangular bladed rotor, with constant NACA23012 airfoil sections. The blade aspect ratio is equal to 16.529 and the linear aerodynamic twist is equal to -8°/R, R being the radius, equal to 2m.

The experimental point chosen for this validation is the baseline case. It is a descent flight in BVI conditions:

- Advance ratio: 0.1512
- Fixed rotor shaft angle: 4.5° aft
- Target lift coefficient: $200C_T/\sigma=11.88$
- Rotor rotating speed: 1041 RPM
- Freestream Mach number: 0.0963

Data available for comparison include blade motion, sectional airloads, tip vortex trajectory visualization through PIV and acoustic noise radiation.

**Figure 1. HART II experiment in DNW wind tunnel**

## 3.2. Meshes

The reference computation and the vorticity confinement one use the same blade mesh illustrated in Figure 2. It is a 3 million point mesh per blade with 194 points in the spanwise direction and 119 points chordwise on the suction and pressure sides.

Both CFD computations were performed using a Cartesian background grid automatically generated using an octree approach [14] with a one over two cell size change between each

Cartesian level. Two different grids where used, the first one is a very refined grid used for the reference computation. It counts 49 million points for a minimum cell size of 0.009mm (7.5% of blade chord). The coarser grid counts only 13 million points for a minimum cell size of 0.014mm (11.6% of blade chord). Both meshes have exactly the same topology (only the cell size in each Cartesian level is different) and they extend in the farfield up to 6 rotor radii.

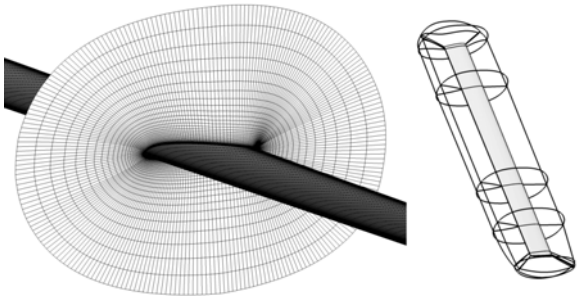

**Figure 2. BO105 blade mesh**

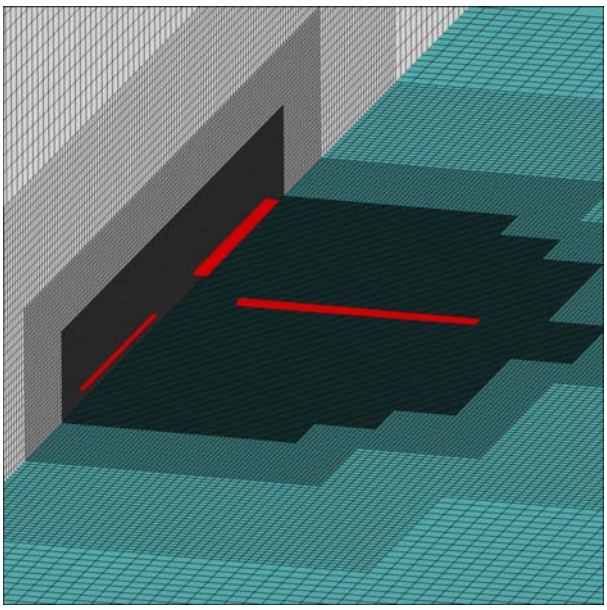

**Figure 3. Coarse background mesh**

Blade surface deformation from the comprehensive dynamics code is propagated by the deformation module of the elsA solver through all the blades meshes at each time iteration. The background grid remains unchanged and boundary conditions are exchanged between the blades meshes and the background grid using an overset grid approach and a two cells layer interpolation.

The computational cost of each computation is directly linked to the mesh size since vorticity confinement adds almost no computational time to the simulation. The CFD computation running on the coarse mesh (with or without vorticity confinement) is approximately three time faster than the fine mesh computation.

To assess the ability of vorticity confinement to limit vortex dissipation on a coarse grid, a first computation without vorticity confinement was run on the coarse mesh, and then two more revolutions where performed using the vorticity confinement method.

Note that while in the experiment there was a fuselage below the rotor, in the computation there is no fuselage neither rotor head.

## 3.3. Rotor trim and blade dynamics

The rotor trim is performed through a loose coupling process for a targeted thrust, rotor shaft angle (which is set to experimental value) and rolling and pitching moment are forced to zero. The trim was not recomputed for the coarse mesh with and without vorticity confinement, but instead, the final trim from the fine mesh loosely coupled simulation was re-used. Postprocessing showed that the difference in thrust (which is the trim objective) between the fine mesh computation and the coarse mesh computation with vorticity confinement is lower than 0.1 %.

Rotor trim at convergence of the loose coupling process is shown in Table 1 for the fine CFD computation and compared to experiment. Trim angles predicted are all within 0.5° of the experimental values, which is a relatively good agreement and similar to what is found in the review paper [15].

| | Experiment | CFD |
|---|---|---|
| $\Theta_0$ (°) | 3.8 ± 0.04° | 3.4190 |
| $\Theta_{1c}$ (°) | 1.92 ± 0.01° | 1.6 |
| $\Theta_{1s}$ (°) | -1.34 ± 0.01° | -0.9635 |

**Table 1. Rotor trim comparison (experiment .vs. computation)**

Figure 4 shows a comparison between experiment and CFD of the blade tip displacement at convergence of the loose coupling iterations. For the experiment, the displacement obtained for the four different blades is shown. It can be seen that the overall blade dynamics is correctly captured by the computation. Some non negligible discrepancies appear on the lead lag angle between roughly 120° and 240° azimuth, on the flap displacement before 60° azimuth and after

230° azimuth and to a lower extend also on the torsion component around 90° azimuth. However, discrepancy on the torsion is partly compensated by the differences in cyclic component of the pitch which result in a reasonnable prediction of the total pitch angle in this area. These discrepancies may affect the vortex strength and pattern and in return the BVI capturing for the following blades.

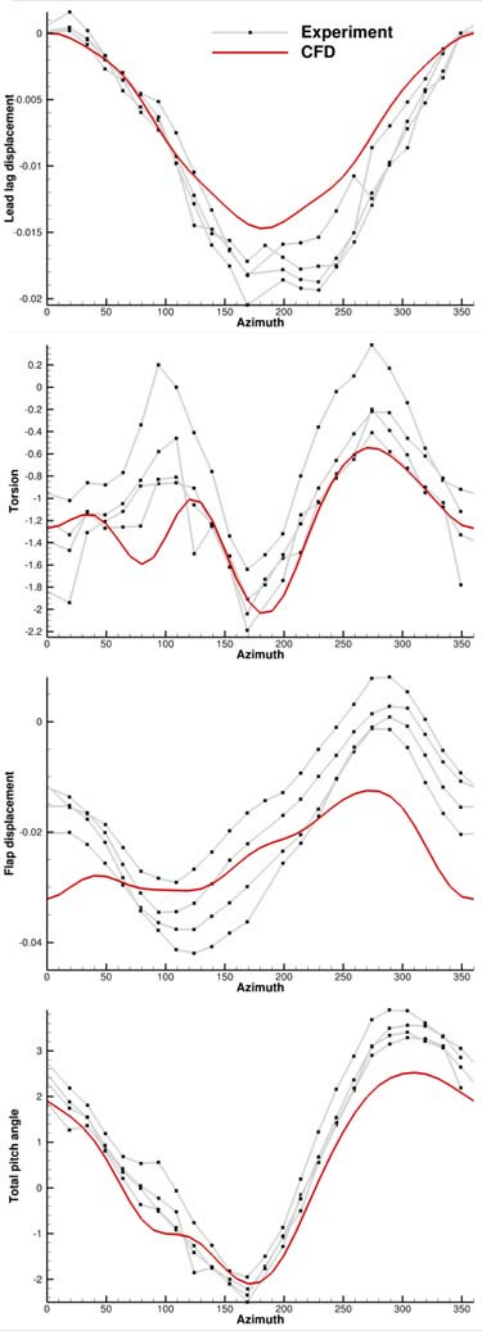


**Figure 4. Blade tip displacement (experiment .vs. computation – from top to bottom: torsion, lead-lag, flap angles and total pitch angle)**

## 3.4. Aerodynamic Analysis

Figure 5 shows the effect of vorticity confinement on vorticity contours in the X, Y and Z planes. It can clearly be seen that a lot of vorticity is lost by the coarse mesh, compared to the fine one, when vortices propagate downstream. The vortex strength on the retreating side is considerably lowered, likely leading to weaker interactions. Adding the vorticity confinement method, enables to propagate most vortices further downstream before they have lost too much of their intensity. However, even if on the retreating side, vorticity confinement enables to almost recover vorticity strength from the fine mesh, on the advancing side the effect is less obvious and the strength of

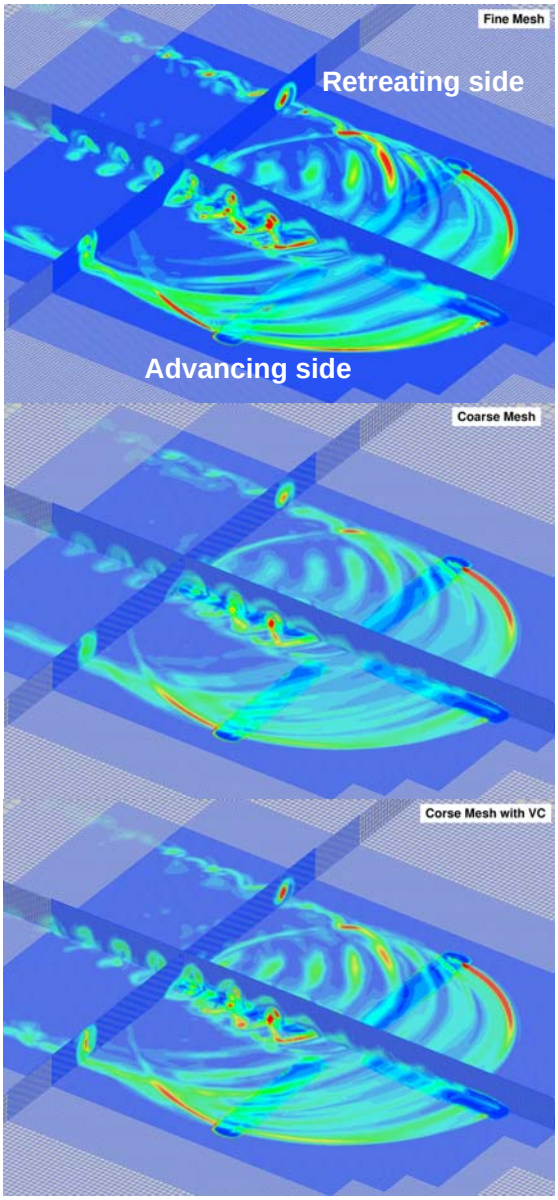


**Figure 5. Effect of vorticity confinement on blade wake and tip vortex**

the vortices remains much lower than on the fine mesh.

Figure 6 shows the fluctuations of the lift coefficient at 87% radius from experiment and from all the computations. Detailed view of advancing and retreating side high frequency fluctuations are shown in Figure 7. The overall blade aerodynamics is correctly captured by all the methods. However, the advancing side features a lower accuracy compared to experiment than the retreating side both in terms of phase and strength of the interactions. The important phase shift observed on the lift between 40° and 220° azimuth may be related to the discrepancies on the blade dynamics that are also observed in this area. It should be noticed that published results indicate that including the fuselage in the computation significantly reduces this phase shift [16].

Lift fluctuations between 20° and 60° azimuth are also relatively low in the computation compared to experiment. These interactions are much more difficult to capture through computation since they are due to vortices slightly older than on the retreating side, and most of all, because of the lower tip loading of the advancing side results in lower tip vorticity shed in the wake. As a result, it is difficult not to dissipate vorticies before the interactions even when a fine mesh is used.

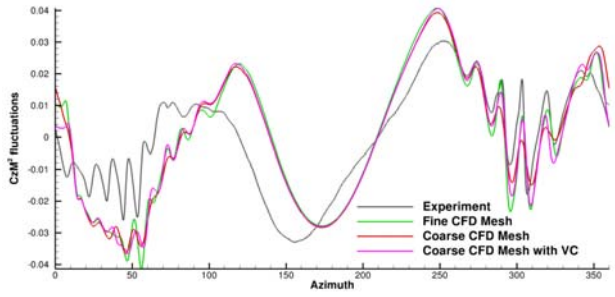


**Figure 6. Fluctuation of lift coefficient at 87% radius (experiment .vs. computation)**

As expected, the fine mesh computation gives much sharper interactions than the coarse mesh. Using the vorticity confinement method tends to increase the blade vortex interactions from the coarse mesh. The levels of fluctuations from the fine mesh are almost recovered on the retreating side by the use of vorticity confinement. However, on the advancing side, the vorticity confinement effect is less beneficial, fluctuations are still lower than the fine mesh predictions between 20° and 60° azimuth. A small phase shift in the interactions positioning is also visible between the vorticity confinement computation and the fine mesh or the coarse mesh computation for some specific interactions either on the advancing or the retreating side. The reason for this phase shift still remains unclear.

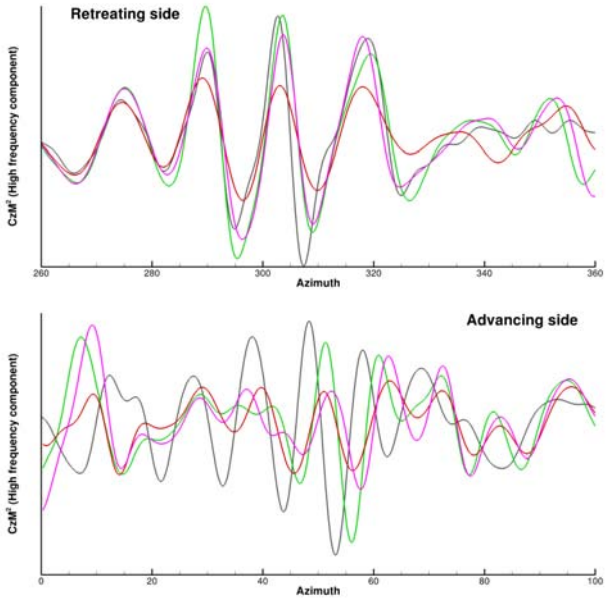


**Figure 7. High frequency component of the lift coefficient fluctuations at 87% radius (experiment .vs. computation)**

In the experiment, flow visualization in order to extract vortex core position in several longitudinal planes was performed by PIV with two different data acquisition setup, one corresponding to the blade position of 70° azimuth and another one for 20° azimuth (Figure 8).

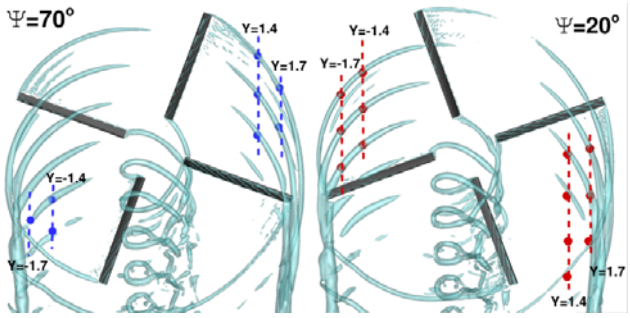


**Figure 8. Overview of the vortex measurement location**

The same postprocessing can be performed in the CFD computations using cuts at constant Y positions in the background mesh and searching for the extremum of vorticity, in order to outline the approximate location of the tip vortex centers. Such postprocessing is compared to experimental values in Figure 9 for Y=+-1.4 and in Figure 10 for Y=+-1.7. The planes at Y positive are for the advancing rotor side and Y negative for the

retreating side, the rotor head center coordinates being equal to (0,0).

Overall the tip vortex positions are very well captured by both CFD methods. While the miss distance between the rotor blade and the tip vortex is slightly underestimated at 1.4 meters on the advancing side, the retreating side is pretty well captured both in terms of tip vortex elevation and position. The shift in the vortex core position on the advancing side for the computation using the vorticity confinement is more questionable since it remains unexplained.

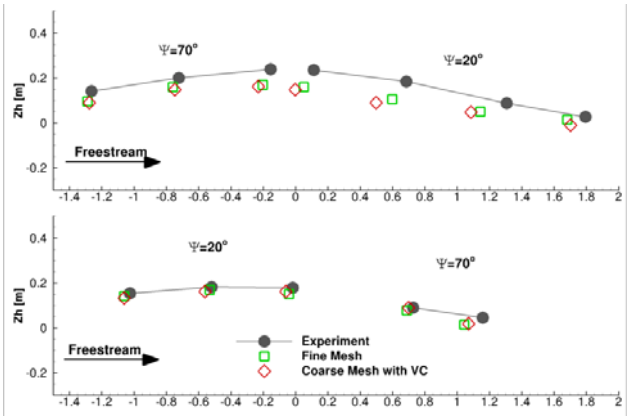


**Figure 9. Vortex location in the longitudinal cutting plane Y=1.4 (advancing side, on top) and y=-1.4 (retreating side, at bottom)**

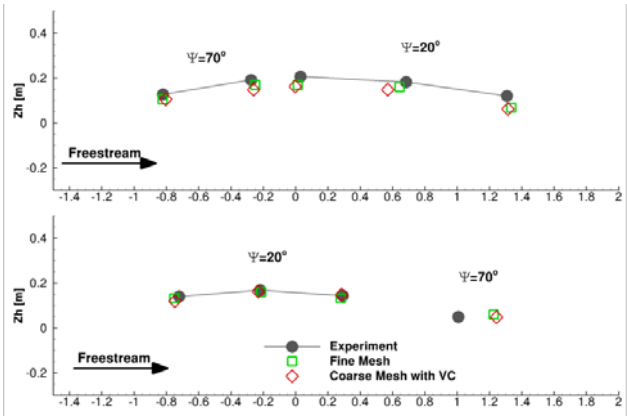


**Figure 10. Vortex location in the longitudinal cutting plane Y=1.7 (advancing side, on top) and y=-1.7 (retreating side, at bottom)**

## 3.5. Acoustic Analysis

Predicted and measured noise footprints are presented in Figure 11. A 6-40 BPF (Blade Passing Frequency) filtering is applied to eliminate low frequency noise and make BVI noise emerges. The wind is coming from the top and the rotor is turning counter-clockwise seen from above. Table 2 summarizes the differences

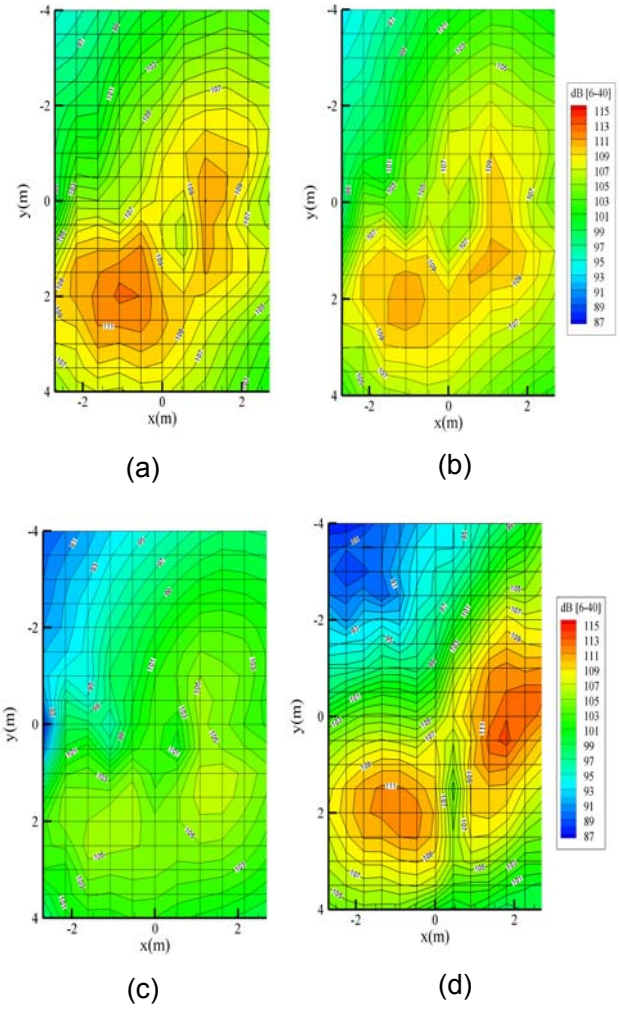


**Figure 11. Noise footprints of the BL case, (a): fine mesh, (b): Coarse mesh with VC, (c): Coarse mesh without VC, (d): Measurement**

| | Fine mesh | Coarse mesh | Coarse mesh with VC |
|---|---|---|---|
| Advancing side | -2.6 dB | -6.9 dB | -3.5 dB |
| Retreating side | +1.4 dB | -5.9 dB | -0.5 dB |

**Table 2. Noise level differences at the maximum noise locations**

in dB at the maximum level location on both advancing and retreating sides of the rotor, the reference being the measured value.

The directivities are characterized by two areas of high noise level, one on the left side corresponding to interactions occurring in retreating side and the other one on the right side corresponding to advancing side interactions. The best results are obtained on the retreating side for all the simulations in terms of directivity and levels.

This is often the case since interacting vortex are younger and more intense. On the advancing side, the underestimation is more important and the shape of the footprint is more oblique on the experimental results. This means that the main interactions predicted by CFD occur later producing a more vertical directivity. The directivity of the noise emission obtained with VC and a coarse mesh is also a bit different on the advancing side from what is computed with the fine mesh. Since the directivities of the noise footprint with and without VC on the coarse mesh are very similar, one can conclude that the change in directivity seems to be due to a too coarse background mesh which changes the wake geometry and consequently the noise directivity. The use of VC does not affect the blade-vortex geometry but only the intensity of the vortex. Thus, a gain of 3.4 dB on the advancing side and 5.4 dB on the retreating side is obtained using VC. However, noise levels are 1 dB lower than the fine mesh computation due in particular to losses of vorticity intensity as already highlighted in the previous section.

## 4. BO105 ROTOR APPLICATION WITH HHC

One objective of the HART II test campaign was to assess the ability of Higher Harmonic Control (HHC) to reduce BVI. Two cases in the same flight condition as the baseline case were run, in order to reduce either acoustic radiations or rotor vibration through the use of HHC.

HHC with 3/rev and blade root pitch control angle of $\Theta_3 = 0.8°$ was applied at a phase of $\psi_3 = 300°$ for the minimum noise case and at a phase of $\psi_3 = 180°$ for the minimum vibration case.

Both cases were analyzed using CFD on the coarse background mesh with vorticity confinement method.

### 4.1. Rotor trim and blade dynamics

Table 3 summarizes the rotor trim obtained at the end of the loose coupling for both minimum noise and minimum vibration cases along with experimental values. Rotor trim accuracy is of the same order as for the baseline case, numerical values are within 0.5° of the experimental ones for all parameters.

Figure 12 and Figure 13 show the comparison of blade tip displacement from experiment and CFD for both cases, the CFD result for the baseline case is also plotted as a reminder. Once again,

| | Minimum noise | | Minimum vibration | |
|---|---|---|---|---|
| | Exp. | CFD | Exp. | CFD |
| $\Theta_0$ (°) | 3.91 | 3.587 | 3.8 | 3.360 |
| $\Theta_{1c}$ (°) | 2.0 | 1.656 | 2.0 | 1.52 |
| $\Theta_{1s}$ (°) | -1.35 | -0.81 | -1.51 | -1.04 |

**Table 3. Rotor trim comparison (experiment .vs. computation)**

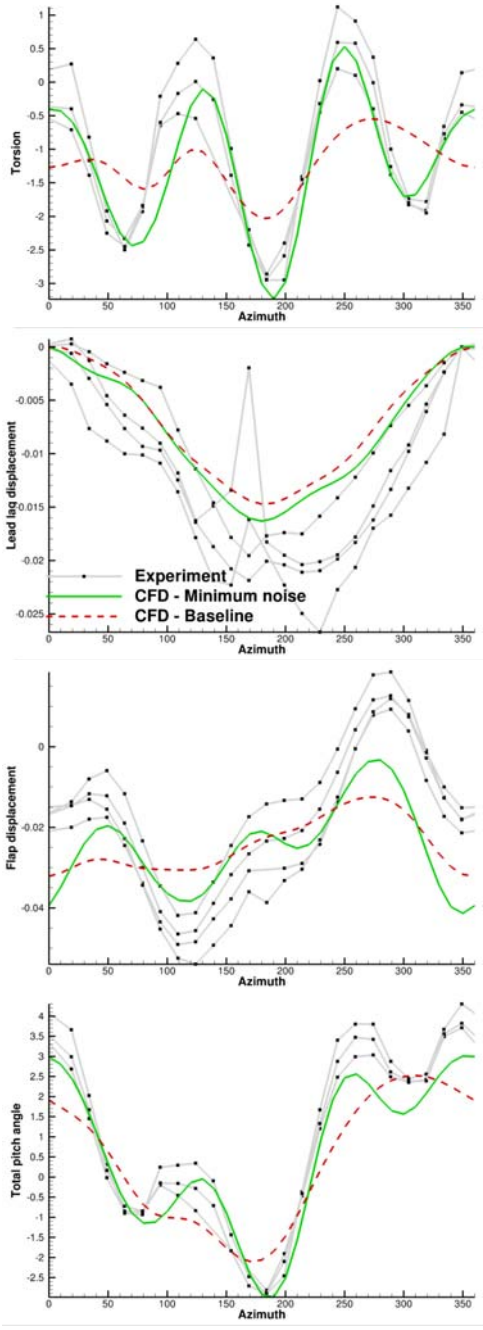


**Figure 12. Blade tip displacement and total pitch for minimum noise case (experiment .vs. computation)**

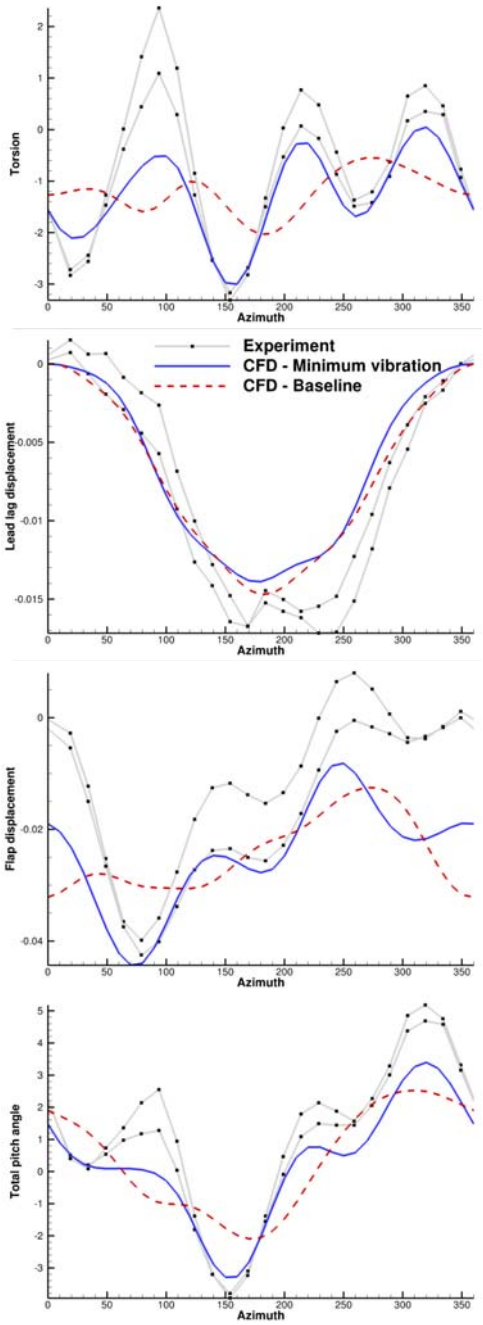


**Figure 13. Blade tip displacement and total pitch for minimum vibration case (experiment .vs. computation)**

the accuracy is similar to the one from the baseline case. There is an overall good agreement in the blade dynamics, with slightly lower accuracy for the lead lag displacement between 120° and 204° azimuth and on the flap displacement before 50° and after 230° azimuth. Concerning the torsion, accuracy is very good for the full revolution and the 3/rev fluctuation due to the HHC is clearly visible. While the lead-lag displacement is not affected by HHC, the response of the flapping displacement is particularly obvious on both minimum noise and minimum vibration cases. It can also be noticed that the difference in phase of the application of HHC between minimum noise and minimum vibration, lead to a different response of the blade flapping, which features much larger oscillations on the minimum noise case than on the minimum vibration case.

## 4.2. Aerodynamic Analysis

Figure 14 shows the lift coefficient time history at 87% of blade radius for experiment (dashed line) and CFD (solid line) for the three HART II cases. A closer view of high frequency fluctuations on the advancing and the retreating side for minimum noise and minimum vibration cases are shown in Figure 15 and Figure 16 respectively.

Overall blade loading is correctly captured for all cases. The increase of fluctuations at 3/rev due to the use of HHC is clearly visible in the

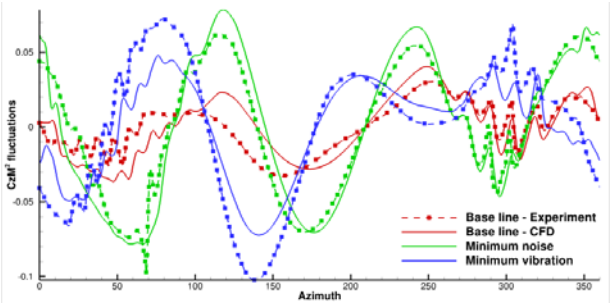


**Figure 14. Fluctuation of lift coefficient at 87% radius (experiment .vs. computation)**

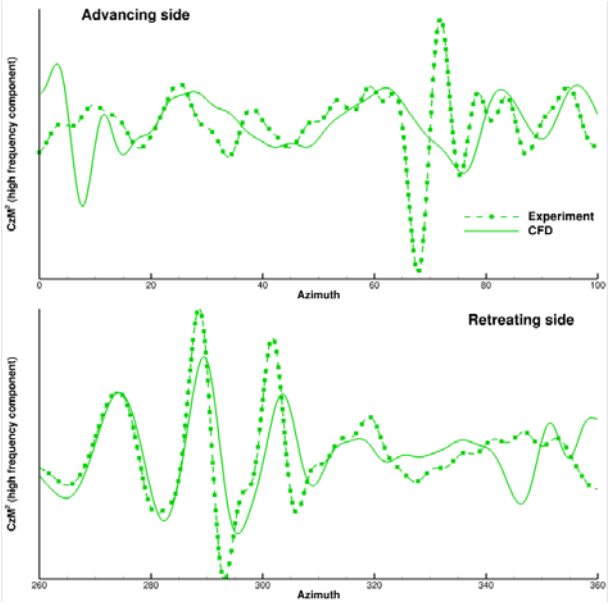


**Figure 15. High frequency component of the lift coefficient fluctuations at 87% radius for minimum noise case (experiment .vs. computation)**

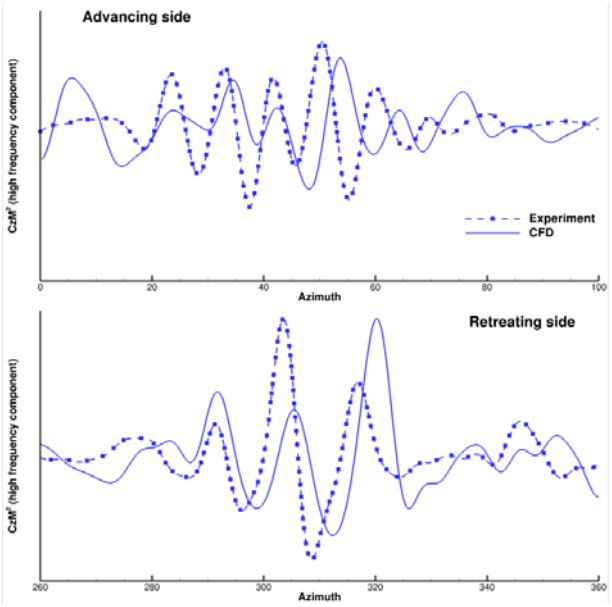


**Figure 16. High frequency component of the liftcoefficient fluctuations at 87% radius for minimumvibration case (experiment .vs. computation)**

computation and they are of the same order as in the experiment. The shift in phase of the low frequency fluctuations between the three different cases is also correctly captured by CFD.

However, as for the baseline case, the advancing side high frequency fluctuations feature larger discrepancies when compared to experiment, both in terms of amplitude and phase. On the minimum noise case, the use of HHC considerably reduces the advancing side interactions in the experiment, making them much difficult to predict for the CFD which features only weak fluctuations.

Figure 17 (respectively Figure 18) compare the tip vortex location in a plane Y=1.4 (respectively Y=1.7) from minimum noise experiment and computation for both advancing and retreating sides. As a reminder the tip vortex location of the baseline case is also shown. As for the baseline case, vortex locations of the minimum noise case are well captured by CFD on the retreating side. However, on the advancing side there are some discrepancies in terms of vortex elevation and position in the longitudinal axis.

What is interesting to note is that the effect of HHC on the downward vortex convection is correctly captured by the CFD on the advancing side even if the CFD seems to underestimate this effect.

Figure 19 compares the tip vortex location for the retreating side in a plane Y=-1.4 and Y=-1.7 from

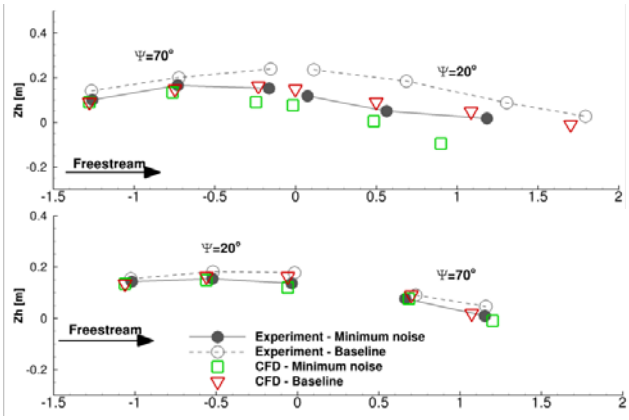


**Figure 17. Vortex location in the longitudinal cutting plane Y=1.4 (advancing side, on top) and y=-1.4 (retreating side, at bottom) for minimum noise case**

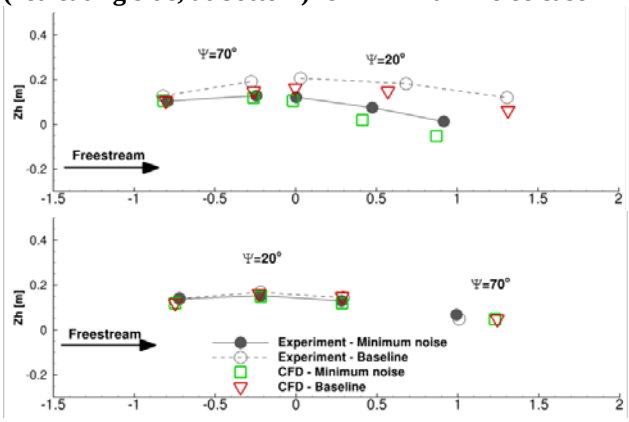


**Figure 18. Vortex location in the longitudinal cutting plane Y=1.7 (advancing side, on top) and y=-1.7 (retreating side, at bottom) for minimum noise case**

minimum vibration experiment and computation. As a reminder the tip vortex location of the baseline case is also shown. As usual, the retreating side vortex positioning is relatively well captured by CFD. The effect of HHC both on experiment and computation is relatively small on the vortex location for the retreating side. Most of the effect of the HHC on the minimum vibration case is actually on the advancing side, which is also the most difficult to predict in CFD even on the baseline case. For the minimum vibration case, experimental data indicates that advancing side vorticity is split in two counter-rotating vortices due to the negative loading at the blade tip at the emission time. However, it is extremely difficult to locate the center of these vortices in the computation (Figure 20, white dots are the experimental vortices centers locations) because of the large number of vortices in this area and also because their strength is relatively small. It seems that the combination of the coarse mesh with vorticity confinement is not able to accurately predict and propagate these counter-rotating vortices. There are several possible explanations

to this behaviour. The mesh may be too coarse, and since the core diameter of two counter-rotating vortices is smaller than the core of a unique vortex as those obtained in the other cases, they are filtered in the overset area between the blade mesh and the background mesh because of too large cells. Note also that the blade mesh, which external cell sizes was adapted to the fine background grid was reuse for the coarse background grid, even if it was not truly adapted to the new cell size. It could also be due to the fact that vorticity confinement is not applied if two neighbouring cells have vorticity vectors with opposite directions and in the vicinity of two counter rotating vortices which are close to each other, there may be too many cells where we do not apply the confinement terms, resulting in a too fast dissipation of vortices due to the coarse mesh. In any case, it is very likely that grid refinement would significantly improve the prediction.

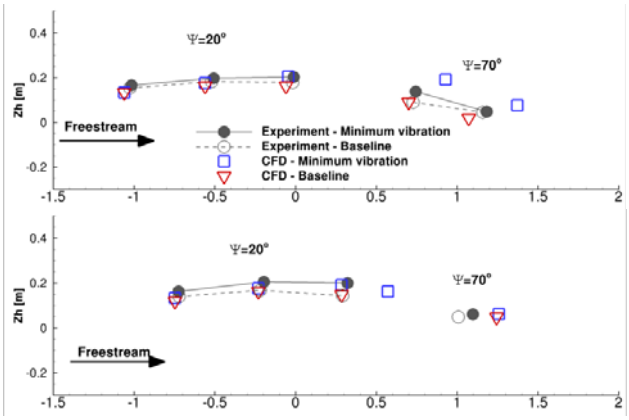


**Figure 19. Vortex location on the retreating side (Y=-1.4 on top, Y=-1.7 at bottom) for minimum vibration case**

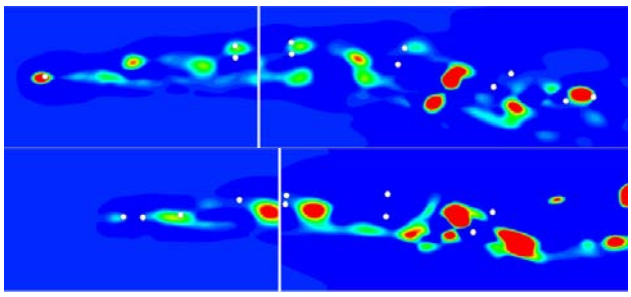

**Figure 20. Vortex location on the advancing side (Y=-1.4 on top, Y=-1.7 at bottom) for minimum vibration case**

## 4.3. Acoustic Analysis

The noise footprints of the MN case filtered on the 6-40 BPF are displayed in Figure 21.

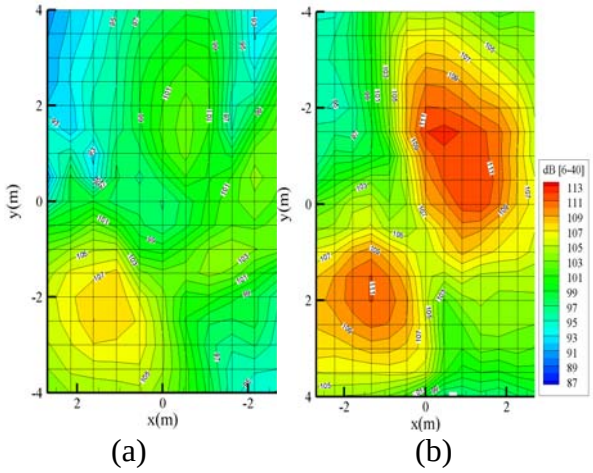


**Figure 21. Noise footprints of the MN case, (a): Prediction, (b): Measurement**

On the retreating side, the predictions are in relatively good agreement with the measurement: the directivity is good, the maxima are located at the same place and the underestimation of the simulations is of 1.8 dB. On the other hand, on the advancing side, the simulated and measured directivities are different. The experimental noise radiation is dominated by one interaction occurring around 70°. This interaction is too weak in the elsA computation. The maximum noise level is underestimated by 8 dB. Actually, it can be demonstrated that the interaction at 70° is predicted more inboard this is why this interaction is not visible in Figure 15. This explains its lower acoustic impact. However, it can be noted that the main interactions occur later during the rotation compared to the baseline case due to a wake located lower in the vertical direction on the advancing side (Figure 17). This is a known effect of the HHC on the MN case that has been well captured by the simulation.

Concerning the MV case, Figure 22 shows the noise carpets obtained numerically and experimentally.

On the retreating side, the maximum noise level is well predicted since the underestimation between the respective maxima is only of 0.6 dB. However, the location of this maximum is located more upstream in the simulation and the area of high noise level is smaller. On the advancing side, the underestimation is more important and equal to 2.3 dB. The predicted directivity is good with an area of high noise level bigger and a maximum shifted on the right of the rotor disc. In this case, the HHC increases experimentally the noise by 3.5 dB on the advancing side and has a small effect on the retreating side interactions by

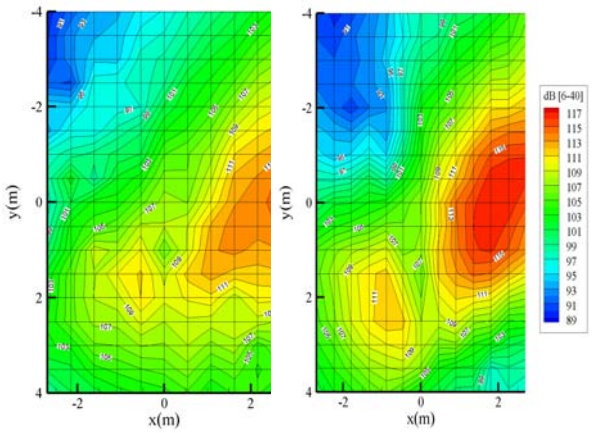


**Figure 22. Noise footprints of the MV case, (a): Prediction, (b): Measurement**

comparison with the baseline case. This effect is well captured by CFD. If one compares to the results obtain in section 3.5 using the same meshes, parameters and VC parameters, a 4.4 dB increase is obtained on the advancing side.

To conclude, even if some discrepancies are visible in terms of directivity (certainly due to differences in terms of wake geometry), the main effect of the HHC on acoustics is captured.

## 5. ERATO ROTOR APPLICATION

The ERATO program [18], [19], [20] launched in 1992, is a cooperation between ONERA, DLR and Eurocopter, aimed at designing and testing an aero-acoustically optimised rotor model, without penalties in terms of consumed power and dynamic loads. This program ended in 1998, with a proof of the design by means of wind-tunnel tests in the DNW and S1MA wind tunnels. The final ERATO design had a very specific planform, with a double sweep concept (forward/backward). This is this final blade shape that is analysed below.

### 5.1. Erato Test Case and meshes

The test case considered in this study is the descent flight case number 399 of the DNW wind tunnel tests characterized by:

- Advance ratio: 0.166
- Target lift coefficient: 12.5
- Target drag coefficient: -1.032
- Rotor rotating speed: 945.7 RPM
- Advancing velocity: 34.5m/s
- Descent angle: -6°

Concerning the CFD simulation, the background mesh is similar to the coarse mesh that was used in previous sections. It counts four levels of refinement with a minimum cell size of 10% of the rotor chord for a total number of points of 24 millions.

Each blade is meshed using multiblock curvilinear O-grid as seen in Figure 23. This grid is composed of 113 points around the chord and 117 points in the spanwise direction and 61 in the wall normal direction for one chord extend, leading to a total of 1.1 million points per blade.

Numerical parameters used for this simulation are the same as the one used for the HART II cases, and already detailed in 2.1.

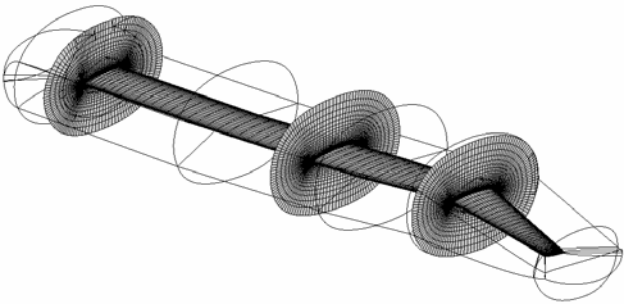

**Figure 23. ERATO blade mesh**

### 5.2. Rotor trim

As in the previous application, the rotor trim is performed through a loose coupling process. However, in the current case, trim is computed using targeted rotor thrust and drag coefficients and longitudinal and lateral cyclic flap are forced to zero ($\beta_{1c}$= $\beta_{1s}$=0.). In this computation, the rotor shaft angle is a degree of freedom, as it was the case during the wind tunnel test.

| | Experiment | CFD |
|---|---|---|
| $\alpha_q$ | 4.3 | 4.1 |
| $\Theta_0$ (°) | 1.765 | 2.83 |
| $\Theta_{1c}$ (°) | 2.737 | 2.01 |
| $\Theta_{1s}$ (°) | -1.834 | -1.50 |

**Table 4. ERATO rotor trim**

Rotor trim at convergence is shown in Table 4. While the shaft angle is correctly captured by the computation, both collective and lateral cyclic pitch are respectively overestimated and underestimated. Note that deficit of lateral cyclic

pitch can be due to the test rig that is not taken into account.

## 5.3. Aerodynamic Analysis

Figure 24, Figure 25 and Figure 26 compare the sectional lift coefficients from experiment, CFD without VC and CFD with VC, for three different blade radii (75% radius, 85% radius and 92.5% radius). The overall blade dynamics is correctly captured by both CFD computations at all radii. On the retreating side, both CFD computation capture high frequency lift fluctuations due to BVI, and using vorticity confinement tends to increase the fluctuations amplitudes. However, retreating side fluctuations in the computations feature some phase differences compared to experiment at all radii and passed 310° azimuth, their amplitude tends to be largely underestimated even for the computation that includes vorticity confinement.

Concerning the advancing side BVI, which is always more difficult to predict, the computation without vorticity confinement features extremely

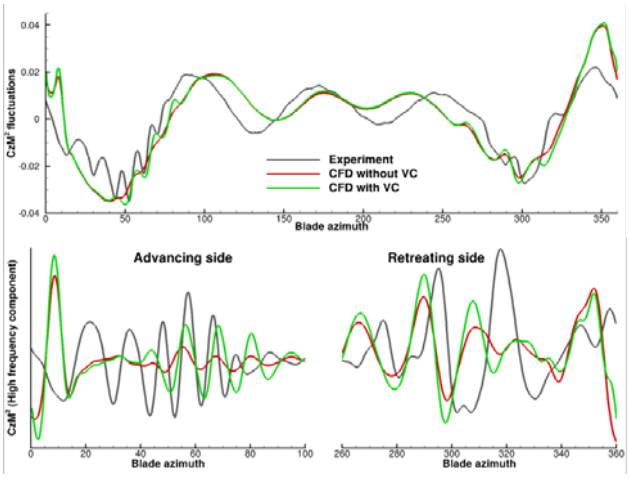


**Figure 24. ERATO lift time history at 0.75R**

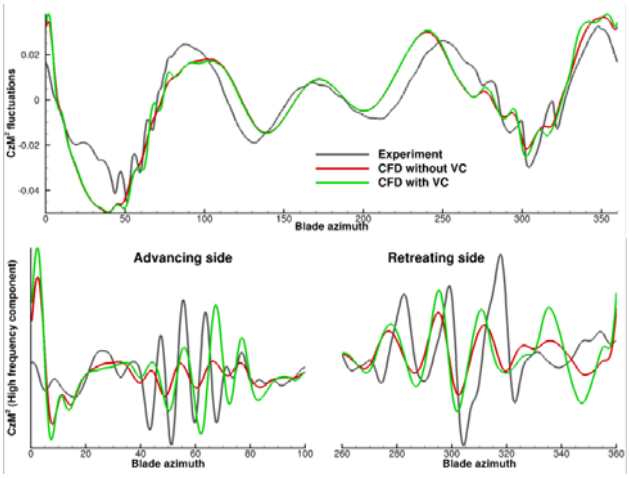


**Figure 25. ERATO lift time history at 0.85R**

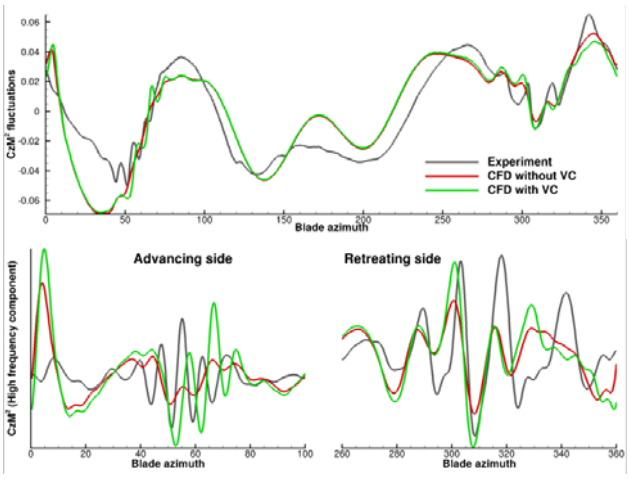


**Figure 26. ERATO lift time history at 0.925R**

weak interactions. Using the VC tends to increase the fluctuations due to BVI, and gives results closer to experiment. However, there is still an underestimation of the interactions and a small phase shift with respect to experiment.

## 5.4. Acoustic Analysis

The code KIM is again used to obtain the noise footprints presented in Figure 28 without VC and in Figure 28 with VC. Measurements are presented in Figure 29. The noise footprints are mainly dominated by a large area of high noise level on the advancing side. The retreating side interactions are hardly noticeable, especially on simulations results. Globally, the directivity and location of maxima are well predicted by simulations. However, the numerical dissipation of the elsA computation without VC is too important, resulting in an underestimation of 8.4 dB on the advancing side. When the VC is used, the underestimation is greatly reduced, up to 1.2 dB on the advancing side and 2.5 dB on the retreating side. These results show particularly well the efficiency of the VC.

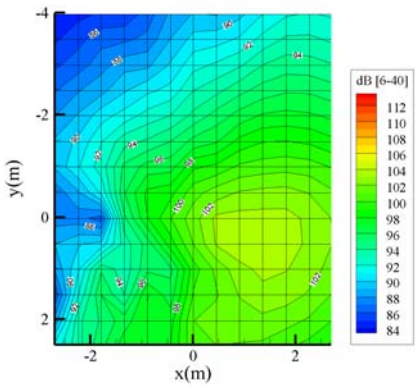


**Figure 27. Noise footprint predicted without VC**

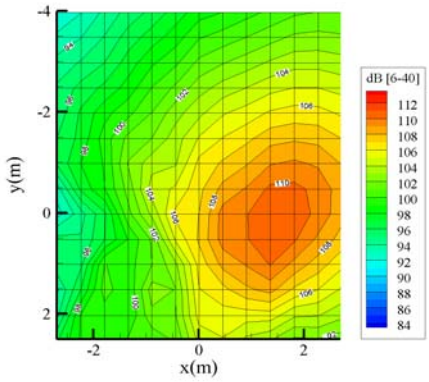


**Figure 28. Noise footprint predicted with VC**

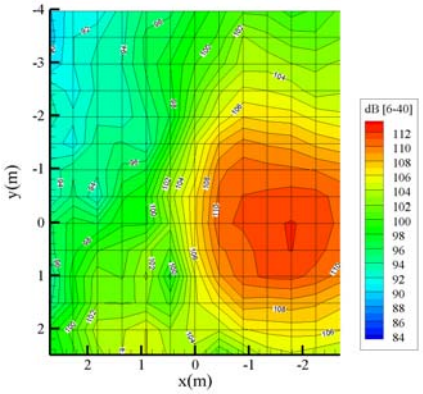


**Figure 29. Noise footprint measured**

## 6. CONCLUSIONS

An aeromechanic and acoustic methodology to predict BVI using CFD was successfully set up. It was shown that the use of vorticity confinement along with a not so refined CFD mesh and a loose coupling with a helicopter dynamics comprehensive code can be a very good alternative with moderate computational cost (three time faster) to a fine mesh computation for BVI prediction.

Vorticity confinement was successfully applied on the three HART II descent flight conditions (baseline, minimum noise and minimum vibration). In all these cases, vorticity confinement computations lead to relatively good prediction of sectional lift fluctuations and noise radiations when compared to experiment.

The same methodology was also successfully applied on ERATO rotor which features a doubly swept planform. Even on this more complex geometry, vorticity confinement enables to accurately predict noise radiation at a moderate cost.

Since vorticity confinement adds almost no extra computational cost, it may also be interesting to use it on an fine background grid to improve even more acoustic predictions.

## ACKNOWLEDGMENTS

This work was completed in the frame of the SHANEL project funded by the French Ministry of Transport (DGAC) and monitored by the Ministry of Defence (DGA).

## REFERENCES

[1] Costes, M., Renaud, T., Rodriguez, B., “Rotorcraft simulations: a challenge for CFD”, International Journal of Computational Fluid Dynamics, Vol. 26, Nos. 6–8, July–September 2012, 383–405

[2] L. Cambier, S. Heib, S. Plot, "The Onera elsA CFD software: input from research and feedback from industry", Mechanics & Industry, Volume 14, Issue 03, 2013, pp 159-174.

[3] Steinhoff, J., Underhill, D., “Modification of the Euler equations for vorticity confinement: application to the computation of interacting vortex rings”, Phys. Fluids 6 (8), 1994.

[4] Steinhoff, J., Fan, M., Wang, L., Dietz, W., “Convection of concentrated vortices and passive scalars as solitary waves”, SIAM Journal of Scientific Computing, VOL. 19, Nos 1-3, 2003.

[5] Costes, M., Juillet, F., “Analysis and higher-order extension of the VC2 confinement scheme “, Computer & Fluids 56 (2012), 102-117.

[6] Costes, M., “Development of a 3rd-order Vorticity Confinement scheme for rotor wakes simulations”, 38th European Rotorcraft Forum, Amsterdam, September 2012

[7] Benoit B., Dequin A-M., Kampa K., Grunhagen W., Basset P-M., “HOST: a General Helicopter Tool for Germany and France“, 56th Annual Forum of the American Helicopter Society, Virginia Beach, May 2000.

[8] Beaumier, P., Costes, M., Rodriguez, B., Poinot, M., Cantaloube, B., “Weak and strong coupling between the elsA CFD solver and the HOST helicopter comprehensive analysis“, Proceeding of the 31st European Rotorcraft Forum, Florence, Italy, 2005.

[9] Prieur, J., Rahier, G., “Comparison of Ffowcs Williams-Hawkings and Kirchhoff rotor noise calculations”, 4th AIAA/CEAS Aeroacoustics Conference, Toulouse, May 1998.

[10] Rahier, G., Prieur., J., “An efficient Kirchhoff integration method for rotor noise prediction starting indifferently from subsonically or

supersonically rotating meshes", AHS forum 53, Virginia Beach, May 1997
[11] Ffowcs Williams, J.E., Hawkings, D.L., "Sound generation by turbulence and surfaces in arbitrary motion" Philo. Trans. Royal Society of London, Vol. 264, A1151, pp. 321-342, May 1696.
[12] Wright, S.E., "The relative importance of acoustic sources generated by helicopter rotors in high speed flight", Second European rotorcraft and Powered Lift Aircraft Forum, Buckeburg, Germany, 1976.
[13] Van der Wall, B., Burley, C., Yu, Y., Pengel, K., Beaumier, P., "The HART II Test - Measurement of Helicopter Rotor Wakes", Aerospace Science and Technology, 2004, Vol 8(4)
[14] Benoit, C., Jeanfaivre, G., "3D inviscid isolated rotor and fuselage calculations using chimera and automatic Cartesian partitioning methods", Journal of the American Helicopter Society, pp. 128-138, April 2003.
[15] Smith, M., J., et all, "And assessment of CFD/CDS Prediction State of the Art Using the HARTII International Workshop Data", 68th annual forum of the American Helicopter Society, Ft. Worth, TX, USA, Mai 2012.
[16] Lim, J. and Dimanlig, A. C. B., "An Investigation of the Fuselage Effect for HART II Using a CFD/CSD Coupled Analysis," Proceedings of the AHS 2nd International Forum on Rotorcraft Multidisciplinary Technology, Seoul, Korea, 2009.
[17] Costes, M., Renaud, T., Rodriguez, B., Reboul, G., "Application of vorticity confinement to rotor wake simulations", Int. J. Engineering Systems Modelling and Simulation, Vol. 4, Nos. 1/2, 2012
[18] Prieur, J., Splettstoesser,W.R., "ERATO - An ONERA-DLR Cooperative Programme On Aeroacoustic Rotor Optimization", 25th European Rotorcraft Forum, Rome, Italy, September 1999.
[19] Splettstoesser, W., Van-der-Wall, B., Junker, B., Schultz, K., Beaumier, P., Delrieux, Y., Leconte, P., P., Crozier, P., "Wind Tunnel Test Results and Proof of Design for an Aeroacoustically Optimized Rotor", 25th European Rotorcraft Forum, Rome, Italy, September 1999.
[20] Delrieux, Y., Prieur, J., Costes, M.,Gardarein, P., Beaumier, P., Mercier des Rochettes, H., Leconte, P., Crozier, P., Splettstoesser, W.R., van der Wall, B., Junker, B., Schultz, K.-J., Mercker, E., Pengel, K., Philippe, J-J., Gmelin B., "The Onera-DLR Aeroacoustic Rotor Optimisation Programme ERATO: Methodology and Achievements", AHS Aerodynamics, Acoustics, and Test and Evaluation Technical Specialists Meeting, San Francisco, January 2002.

## COPYRIGHT STATEMENT